

Impacts of nucleating aerosol on anvil-cirrus clouds: A modeling study

G.G. Carrió *, S.C. van den Heever, W.R. Cotton

Department of Atmospheric Science, Colorado State University, Fort Collins, Colorado 80523-1371, USA

Received 24 January 2006; received in revised form 29 June 2006; accepted 29 June 2006

Abstract

This paper examines the potential effects of Saharan dust intrusions on the microphysical structure and optical properties of anvil-cirrus clouds. A series of 3-D LES simulations were initialized and forced by output data from mesoscale simulations in a previous study, in which we analyzed the impact of the enhanced low-level concentrations of cloud-nucleating aerosols on the characteristics of convective storms. The effects of enhancing aerosol concentrations on the ice-particle size distributions as well as some of their moments were analyzed as the LES model domain followed the trajectory of the simulated cirrus cloud. The experimental design was based on aerosol concentrations observed over the peninsula of Florida toward the end of the CRYSTAL-FACE field campaign held during July 2002.

Results indicate that variations in the concentrations of nucleation aerosols have a significant effect on the optical properties and lifetime of cirrus anvil clouds. In addition, enhancing low-level aerosols can affect the radiation budget, leading to surface radiative cooling. Both IFN and CCN enhancements show important effects; however, results suggest that CCN and GCCN play a more dominant role.

© 2006 Elsevier B.V. All rights reserved.

Keywords: Saharan dust; Cirrus; LES simulation

1. Introduction

The radiative effect of tropical high-level clouds is of major importance to the earth's energy budget and climate (Ramanathan and Collins, 1991; Fowler and Randall, 1994; Stephens, 1998). Several studies have indicated that the impact of cirrus clouds on the visible and infrared radiation properties strongly depends on the ice water content (IWC), and size distributions (Platt and Harshvardhan, 1988; Platt, 1989; Jensen et al., 1994).

However, the research community has no consensus as to whether cirrus clouds have a positive or negative feedback on the greenhouse effect (Chou et al., 2002; Lin et al., 2002). Mineral dust, produced by wind erosion of arid and semiarid land areas, is believed to be important in climate processes. Nonetheless, it has been difficult to quantify the effects of dust on climate because of the complex and highly uncertain effect of dust on radiative forcing (Chiapello et al., 2005). Further analyses of the dust effects on cumulus and anvil-cirrus clouds are necessary due to the global extent of transported Saharan dust and the apparent increased frequency of African dust storms (DeMott et al., 2003). Most modeling studies that have focused on tropical

* Corresponding author. Tel.: +1 970 491 8508; fax: +1 970 491 8449.
E-mail address: carrio@atmos.colostate.edu (G.G. Carrió).

cirrus concentrated on their representation in cloud-resolving models (Kreueger et al., 1995; Fu et al., 1995), on their microphysical properties (Brown and Heymsfield, 2001) but not on their sensitivity to variations of aerosol concentrations. Fridlind et al. (2004) coupled cloud simulations with aerosol and cloud particle measurements in convective storm systems during CRYSTAL-FACE field campaign. Their results indicate that most anvil crystals form on mid-troposphere rather than on boundary layer aerosols. Furthermore, their results suggest that distant pollution sources may have a greater effect on these clouds than do local sources.

High concentrations of Saharan dust were observed over the peninsula of Florida during the Cirrus Regional Study of Tropical Anvils and Cirrus Layers-Florida Area Cirrus Experiment (CRYSTAL-FACE) field campaign held during July 2002. The work presented here is a continuation of a previous modeling study (van den Heever et al., 2006) in which the impact of variations in aerosol concentrations on convective storm characteristics over Florida was investigated. Vertical profiles of cloud condensation (CCN), giant CCN (GCCN), and ice forming nuclei (IFN) obtained on “dirty” and “clean” days during the CRYSTAL-FACE field campaign were used as benchmarks for a series of numerical experiments in which the concentrations of these aerosol species were systematically varied. Results demonstrated that variations in the concentrations of lower tropospheric CCN, GCCN and IFN influenced the microphysical and dynamical characteristics of convective storm development over Florida. As expected, nucleation mechanisms played a negligible role after the anvil-cirrus cloud detached from the storm outflow. However, higher concentrations of cloud-nucleating aerosols resulted in significant differences in both microphysical characteristics of the storm outflows as well as the bulk water flux provided by the convective cores. Nonetheless, uncertainties remain as to how do dust intrusions influence radiative properties of anvil-cirrus clouds. To address this question it is necessary to adequately resolve the dominant energy-containing eddies as well as the various microphysical mechanisms important in determining the optical depths and the ice particle size distributions as the anvil-cirrus is advected downwind from the convective impulse. Cheng et al. (2001) used a 3-D LES version of the Regional Atmospheric Modeling System (RAMS) to compare cirrus observations with simulated cloud properties. LES models have been widely used to investigate the formation, maintenance and dissipation of various types of clouds, to develop parameterizations of boundary-layer clouds or turbulent closure models, to evaluate the

sensitivity of model results to parameter changes, as well as to investigate the role of microphysical mechanisms. For most of these studies, the LES domain is seen as a column model capable of generating a realistic statistical perspective of the in-cloud small-scale inhomogeneities affecting microphysical processes and cloud radiative properties. The domain represents a vertical cloud column located far from the cloud lateral boundaries. In particular, several studies have used this LES philosophy to investigate the effects of aerosols on radiative properties of stratiform clouds (Feingold et al., 1994; Harrington et al., 1999; Jiang et al., 2000, 2001; Carrió et al., 2005a,b).

The present paper is a modeling study of the impact of Saharan dust intrusions on the microphysical structure and optical properties of anvil-cirrus clouds. To examine the potential radiative feedback effects, it was necessary to emphasize the differences in the temporal evolution of the storm outflow induced by variations of lower-tropospheric cloud-nucleating aerosols processed within the convective core. For this purpose, we performed a series of 3-D LES simulations in which the domain follows Lagrangian trajectories predicted by the mesoscale simulations (van den Heever et al., 2006). In order to capture the initial microstructure of anvil-cirrus clouds, each LES simulation was initialized with microphysical and thermodynamic profiles that corresponded to the times and locations at which the cirrus-anvil clouds was detached from the storm outflows. Additionally, mesoscale output data were used to define large-scale tendencies for the LES moving domain. The effect of dust intrusions on the ice-particle size distribution and some of its moments have been analyzed. A brief description of the model we used is given in Section 2. In Section 3 we consider the design of the numerical sensitivity experiments and initial conditions. Results, and summary and conclusions are presented in Sections 4 and 5, respectively.

2. Model description

The model used for this study is the LES version of RAMS (Pielke et al., 1992; Cotton et al., 2003) developed at Colorado State University (RAMS@CSU). The dynamic, microphysical and radiative modeling framework in these LES simulations is essentially the same used for part I, differing only in model configuration (see Section 3). This non-hydrostatic model integrates predictive equations for the wind components, the Exner function, the ice–liquid water potential temperature, and the total mixing ratio on a vertically stretched Arakawa C-grid.

The two-moment microphysical framework (Meyers et al., 1997; Saleeby and Cotton, 2003) predicts the mass mixing ratios and number concentrations of various hydrometeor species. It considers two separate modes of cloud droplets that are independently nucleated via activation of CCN and GCCN, using look-up tables derived from a Lagrangian model developed by Feingold et al. (1994). Aerosol particles falling into the size range of 1 to 50 μm are considered as GCCN and activated as drizzle drops. This large-cloud-droplet mode, in combination with the traditional single mode of cloud droplets, permits representation of the bimodal distribution of cloud droplets that is often seen in clouds (Hobbs et al., 1980). This detailed microphysical framework is of great importance for this study as it allows a better representation of numerous microphysical mechanisms (CCN and GCCN activation, homogeneous freezing nucleation, secondary ice production through the Hallett–Mossop processes, and collisions with ice species) affecting the microphysical structure of the storm outflow.

The predicted microphysical variables include the number concentrations and mixing ratios of cloud droplets, drizzle drops, rain, pristine ice, snow, aggregates graupel and hail, as well as the IFN, CCN and GCCN concentrations. These aerosol concentrations can be defined as a vertically and/or horizontally heterogeneous variable that can be advected and diffused

(Cotton et al., 2003). Snow is defined as larger pristine ice crystals ($>100 \mu\text{m}$), which have grown by vapor deposition and riming, while aggregates are defined as ice particles formed by collision and coalescence of pristine ice, snow or other aggregates. Ice crystals are nucleated by heterogeneous nucleation based on a modified formulation of Meyers et al. (1997) which contains the prognostic variable NI as described in van den Heever et al. (2006). In addition, homogeneous freezing of cloud droplets and haze particles is done following DeMott et al. (1994). Supercooled raindrops freeze by collecting ice crystals. Ice multiplication by rime-splinter process is parameterized following Mossop (1978) as described in Cotton et al. (2003). A two-stream radiative transfer model is used for this study (Harrington et al., 1999). The two-stream model solves the radiative transfer equations for three gaseous constituents, H_2O , O_3 , and CO_2 and the optical effects of the hydrometeor size spectra. Gaseous absorption is calculated by following the fast exponential sum fitting of transmissions method proposed by Ritter and Geleyn (1992). Lorenz–Mie theory is used to compute the optical properties for water drops, while the theory of Mitchell et al. (1996) is used for non-spherical ice crystals. For each hydrometeor species, the band-averaged values of optical properties are computed for the assumed gamma distribution basis function following the method of Slingo and Schrecker (1982).

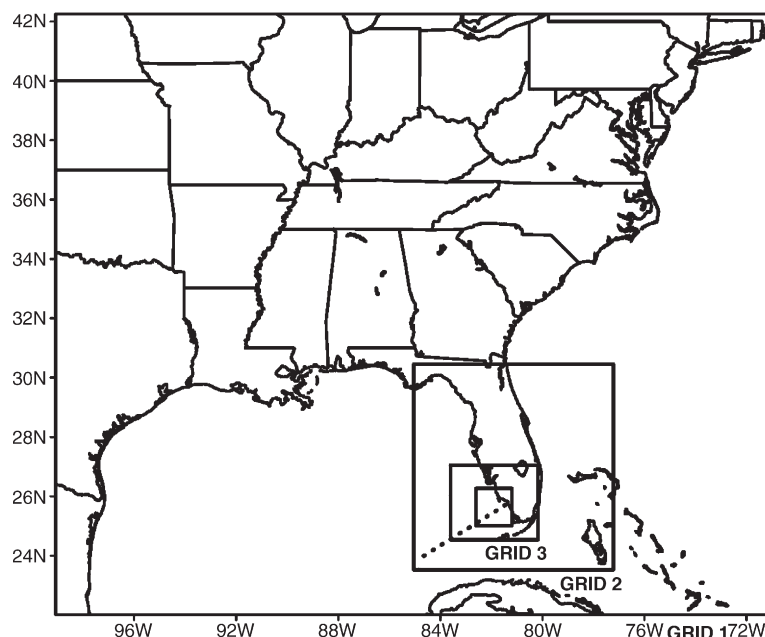


Fig. 1. The locations of grids 1, 2, and 3 of the meso-scale simulations. The dotted line approximately describes the simulated cirrus-anvil trajectories.

3. Model configuration and experiment design

3.1. Mesoscale simulations

As mentioned in Section 1, numerous mesoscale simulations were performed to analyze the response of the convective development to varying aerosol concentrations as well as to provide initial and time-evolving conditions for the LES model. These mesoscale sensitivity experiments were performed using RAMS@CSU with four two-way interactive nested model grids and horizontal resolutions of 50, 10, 2 and 0.5 km. The corresponding domain sizes are: 3000×2500 km, 820×820 km, 350×294 km, and 145×145 km, respectively. The location of the grids is given in Fig. 1. Thirty-six vertical levels with variable grid spacing were used, and the model top extended to approximately 20 km above ground level. The model was heterogeneously initialized with 40 km ETA data from 28 July 2002. An extensive description of the model configuration used for these mesoscale simulations is included in van den Heever et al. (2006). Different aerosol profiles based on measurements obtained from the CRYSTAL-FACE field campaign were used for the design of the various sensitivity experiments (described in Section 3.2). Fig. 2 shows the idealized CCN, GCCN, and IFN profiles used to characterize clean and observed concentrations. While IFN, CCN, and GCCN concentrations were initialized horizontally homogeneously, they then can vary both vertically and horizontally in time following processes such as aerosol activation, nucleation, scavenging, cloud evaporation, advection, diffusion and precipitation. For each numerical experiment, we stored the microphysical and thermodynamic profiles corresponding to the time and location that the cirrus-anvil cloud detached from the storm outflow, as well as those of the corresponding trajectory. In order to illustrate the trajectory of the cirrus-anvil cloud simulated in grid 3 between 20:45 and 23:45 UTC (July 28), Fig. 3 gives the ice water paths between 9 and 14 km for the mesoscale experiment initialized with the observed aerosol concentrations. The further displacement of this cloud (within grid 2) is shown in Fig. 4. This figure gives the ice paths simulated within grid 2 between 00:45 and 03:45 UTC (July 29) for the mesoscale experiment initialized with the observed aerosol concentrations.

Storms initially developed to the south and southwest of Lake Okeechobee, continued to strengthen, accompanied by the development of new convection, and progressed in a westward to southwestward direction,

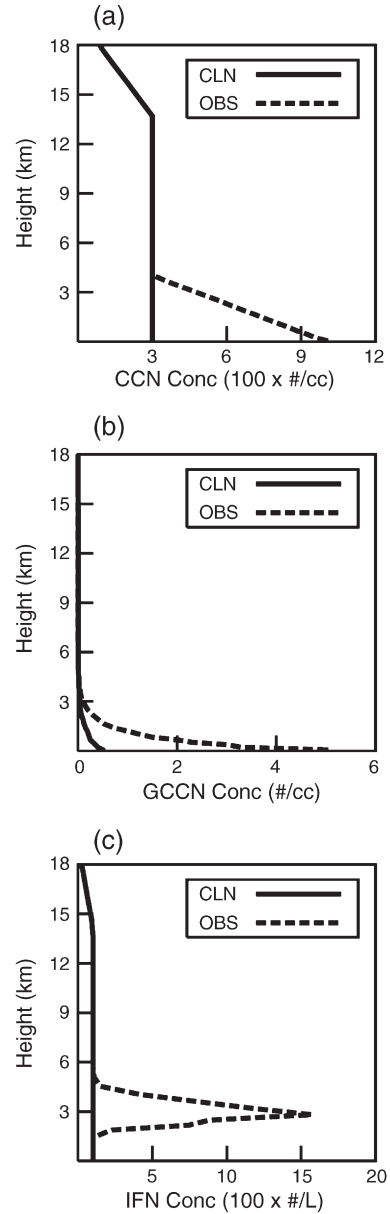


Fig. 2. Idealized vertical (a) CCN, (b) GCCN, and (c) IN profiles used to initialize the meso-scale model.

reaching the coastal regions of Everglade City and Fort Meyers between 2100 and 2200 UTC. Convection started to weaken after ~ 2200 UTC, leaving the remnant anvils extending over the oceans for several more hours. Figs. 5 and 6 are analogous to Figs. 3 and 4, and show infrared satellite imagery at approximately hourly intervals between July 28 20:45 and July 29 03:45 UTC. Even though the trajectories simulated for different sensitivity experiments were very similar, the speed of displacement of the simulated anvil-cirrus

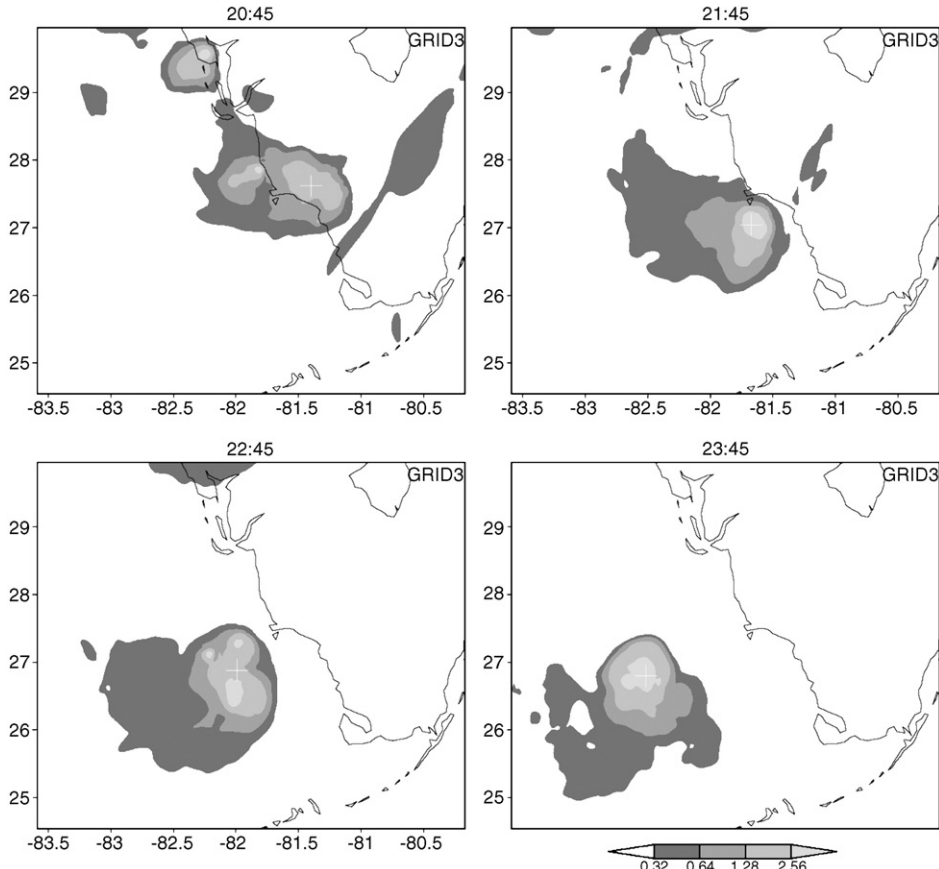


Fig. 3. Vertically integrated condensate simulated in grid 3 for 20:45, 21:45, 22:45, and 23:45 UTC July 28. Ice water paths are expressed in millimeters, correspond to the 9–14 km layer, and the experiment initialized with the observed aerosol concentrations. The cross denotes the position of the LES domain.

clouds slightly changed, as the altitude of the ice content maxima and the cloud depths varied. Additionally, the convection in all simulations tends to move offshore slightly faster than was observed (for more details see van den Heever et al., 2006).

3.2. LES cirrus simulations

This series of LES simulations has been performed in a 3-D framework, using a $5 \times 5 \times 17$ km grid of $100 \times 100 \times 116$ grid points with horizontal grid spacing of 50 m. A constant vertical resolution of 50 m was used for a 4 km layer containing the cirrus-anvil cloud. However, vertical grid spacing gradually increased above and below this layer (Fig. 7). A time step of 2 s was used for all numerical experiments. As mentioned in Section 1, the LES domain represents a column model capable of generating a realistic statistical perspective of the in-cloud small-scale inhomogeneities affecting microphysical processes and cloud radiative properties.

As is common in LES, periodical boundary conditions were applied to control sinks and sources of momentum, water mass, and energy during the course of the simulations, and the domain top was a rigid lid. Rayleigh damping was used in the six highest levels of the domain to prevent the reflection of vertically traveling gravity waves off this rigid lid. Two-moment microphysics was employed for all the water species (pristine ice, snow, aggregates, graupel, hail, cloud water and rain).

LES simulations were initialized at 21:00 UTC on July 28, 2002 with horizontally homogeneous profiles of the mixing ratios and number concentrations of all water species, and thermodynamic variables provided by the finest grid of the corresponding mesoscale experiments. In each case, these vertical profiles correspond to the horizontal position and time at which the cirrus-anvil cloud detached from the storm outflow. A spin-up time of approximately 4 h was considered in order to allow the development of an eddy

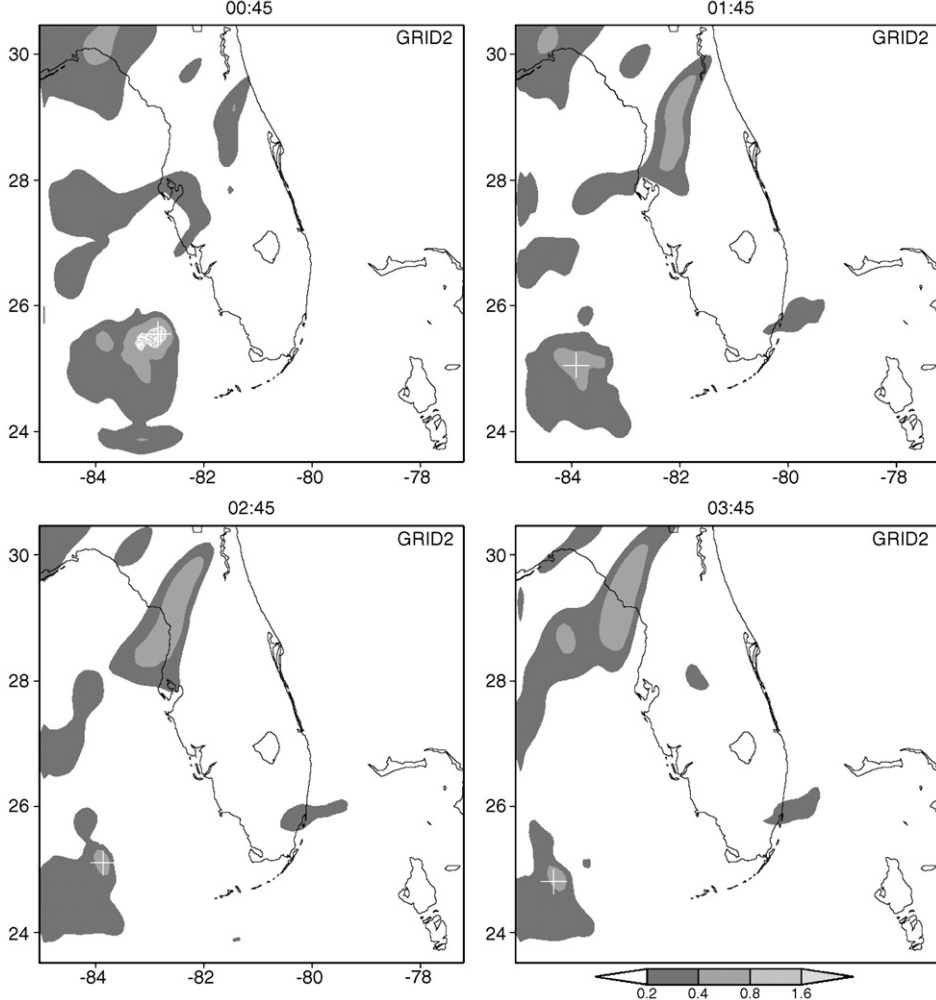


Fig. 4. Idem Fig. 3 but simulated in grid 2 for 0:45, 1:45, 2:45, and 3:45 UTC July 29.

distribution physically consistent with the initialization profiles. During the spin-up time, model time was “frozen”: solar angles did not change and large-scale tendencies were not applied. Additionally, until the model developed stable turbulent statistics, the initialization profiles are also nudged to suppress significant microphysical changes in the horizontally averaged vertical profiles.

For most of the simulations, the duration was 4 h beyond spin-up time. However, we performed two longer simulations (8 h) extending the large-scale tendencies with grid 2 output data. A Newtonian relaxation technique (nudging) was used to define the time-evolving boundary conditions of the LES domain as it moved along the trajectory. These nudging terms were based on the stored vertical profiles of the total water mixing ratio (r_t), horizontal wind components (u ,

v), and the ice–liquid potential temperature (Θ_{il}) corresponding to the mesoscale outputs every 15 min. Nudging was only applied to horizontal averages to avoid nudging out the fine-scale features developed in the LES domain. The scheme used to take into account the large-scale tendencies of r_t , u , v , and Θ_{il} is given in Eq. (1):

$$\begin{aligned} \psi(k,i,t) = & \psi(k,i,t-\Delta t) + \text{model} \\ & + \alpha[\psi_{\text{meso}}(k,t-\Delta t) - \psi_H(k,t-\Delta t)] \end{aligned} \quad (1)$$

where $\psi(k,i,t)$ is the predicted value of a nudged variable at the end of the current time step, $\psi(k,i,t-\Delta t)$ is the model value at the end of the previous time step, where the model includes advection, diffusion, thermodynamic effects, etc., $\psi_{\text{meso}}(k, t)$ is the vertical profile being nudged to and is a function of the vertical index

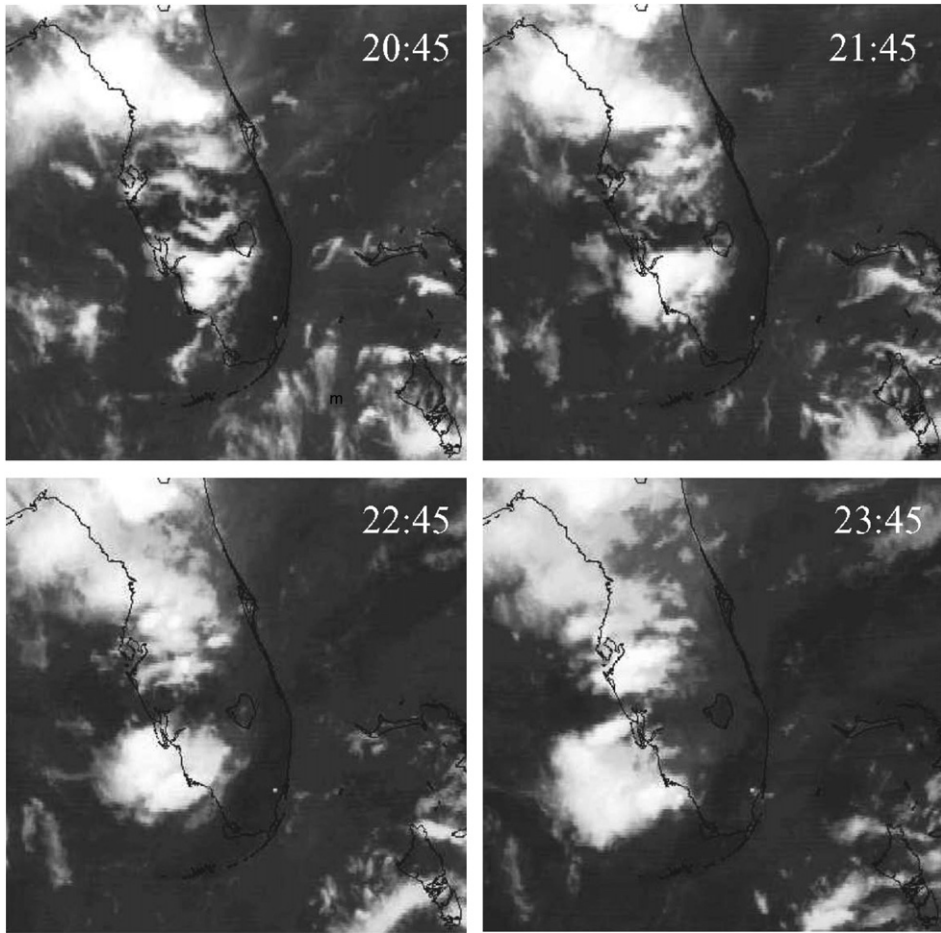


Fig. 5. Infrared satellite imagery (GOES-8, 10.7 μm) at hourly intervals on 28 July 2002 (figures used with the permission of Louis Nguyen, NASA Langley Research Center).

k , $\psi H(k, t - \Delta t)$ is the horizontal average of ψ at the end of the previous time step, and α denotes a nudging intensity.

A list of the cirrus LES runs that correspond to the results presented in this paper is given in Table 1. As LES simulations were initialized with mesoscale output data, the experimental designs of these two series of numerical experiments were obviously linked. Prefixes in the LES experiment names denote the mesoscale experiment initialized with enhanced concentrations of CCN and GCCN (C), all aerosol species (A), and IFN (I). Suffixes 25, 50, and 100 refer to 25, 50, and 100% of the actual concentrations observed on July 28, 2002, respectively.

4. Results

The microphysical module for the LES simulations was configured identically to the finest grid of the

mesoscale simulations: two-moment microphysics for all water species. However, neither liquid-phase hydrometeors nor graupel or hail particles were present in the simulated storm outflows. Therefore, only the water contents of pristine ice, snow, and aggregates (IWC, SWC, and AWC, respectively) were non-negligible at anvil levels. Fig. 8 compares the water contents of these three species, the total ice water content, and total ice particle concentration (N_i) corresponding to the control run (clean), and experiments A50 and A100. All these curves represent the temporal evolution of cloud-averaged values computed using LES outputs every 5 min. Previous studies (e.g., Starr and Cox, 1985) suggest that the vertical transport of ice due to sedimentation was very significant in cirrus clouds. This is especially important for anvil-cirrus clouds as their ice-particle size distributions are expected to be wider. Both the total ice water content and N_i decreased with time (Fig. 8a and b, respectively) as the

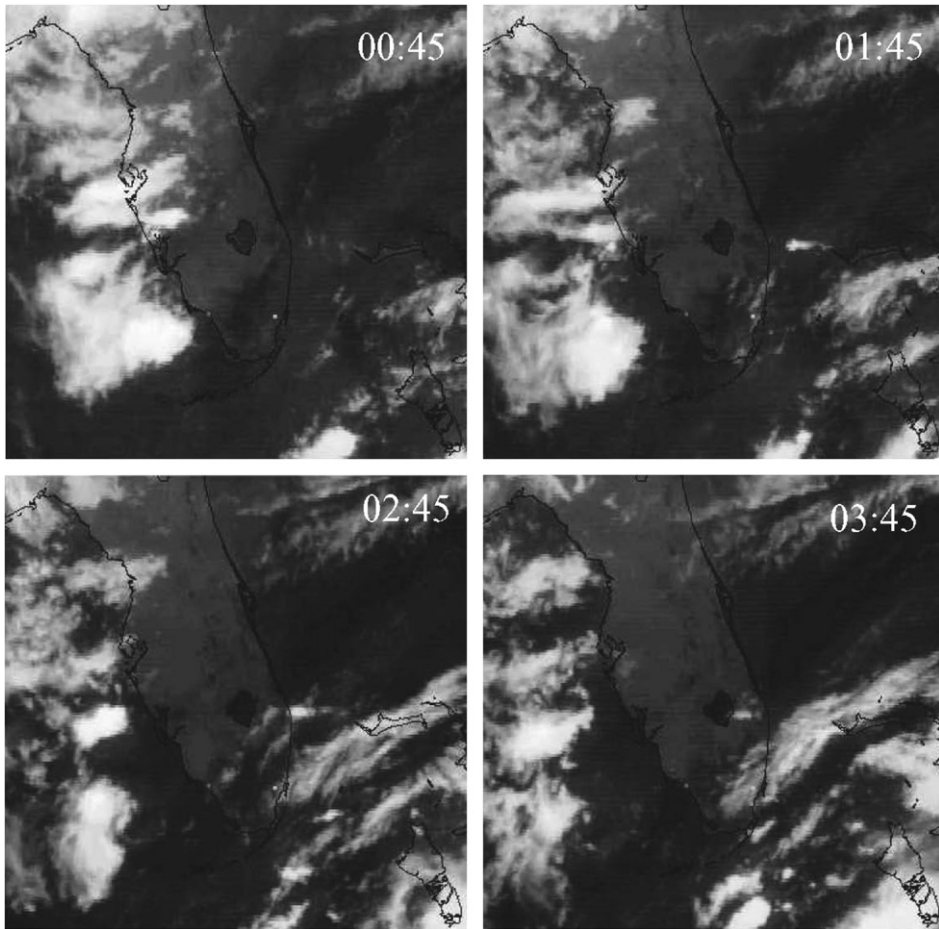


Fig. 6. Infrared satellite imagery (GOES-8, 10.7 μm) at hourly intervals on 29 July 2002 (figures used with the permission of Louis Nguyen, NASA Langley Research Center).

sedimentation of large particles out of the cirrus-anvil cloud produced a dramatic change in the water contents during the first hour of the simulation. At the beginning of the simulation, the total ice water content simulated for A100 was approximately 75% larger than that of the control run. This difference rapidly decreased during the first hours of the simulation although it remained approximately constant (20%) during the last hour. This faster decrease for the sensitivity experiments was associated with a greater mass fraction of particles with larger terminal fall speed (aggregates). Initially, more than one third of the mass corresponded to aggregates for A100, while the corresponding fraction for the control run was approximately 18% (Fig. 8e). Conversely, N_i slightly decreased with time for experiment A100, remaining over 40% above the control run for the entire simulation period (if we compare the number concentration maxima, located near the cloud tops, this difference can exceed 70%, not shown). The

enhancement in N_i was induced through convective storm dynamic forcing as negligible nucleation occurred during the LES simulations. The water contents of all ice-phase species exhibited a clearly monotonic behavior when dustier environments were considered. However, the most affected particles were those formed by the collision and coalescence of small hydrometeors (aggregates). This could be explained as the liquid mass would be distributed in a larger number of cloud droplets and a higher concentration of pristine ice crystals would be activated when more CCN and IFN are available, respectively. When comparing sensitivity experiments with the control run, it can be seen that the relative differences in the total ice water path (Fig. 8f) were more important than those of the total ice water content as the outflows were also deeper. Therefore, enhancing the concentrations of low-level cloud-nucleating aerosol affected not only the bulk water flux provided by the convective impulse but also the

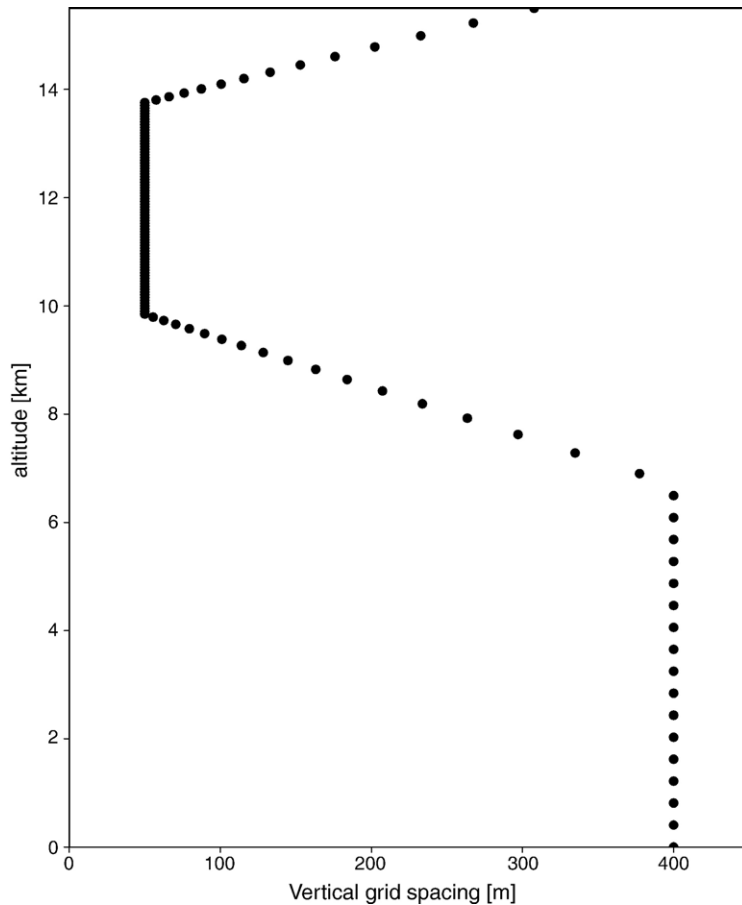


Fig. 7. Vertical grid spacing used for the LES simulations.

microphysical structure of the outflow. The latter affected the temporal evolution of the size distributions and therefore the time-averaged optical and radiative properties of the anvil-cirrus clouds.

From an LES perspective, we modeled the ice particle spectrum binning all two-moment distributions into 500 size categories for each ice-phase species at each cloudy grid cell. These size distributions were

computed every 5 min of simulation and were used to compare time-averaged characteristics and temporal evolutions (see also Fig. 16) for the control run and sensitivity experiments. Simulated density functions ($n(D)$) corresponding to two time periods are compared to Fig. 9 for the control run, A50 and A100. For the entire simulation period (panel a), the magnitude of the mode monotonically increased when more polluted environments (at low-levels) were assumed. However, no significant change in the position of the mode is visible in this figure for different runs. When comparing the distributions obtained for the last hour of the simulations, the magnitude of the modes also varied monotonically when comparing the control run, A50 and A100, and exhibited a more important relative change. In this case, they corresponded to slightly smaller diameters when assuming more polluted environments. Differences (with respect to the control run) were not restricted to small ice particles, the relative change was also important in the tail of the distributions. Percent differences with respect to the control run are given in

Table 1

Aerosol initialization profiles, *clean* and *obs* denote clean concentrations and those observed for July 28, 2002, respectively

Experiment	IN	CCN and GCCN
Control	Clean	Clean
A25	25% obs	25% obs
A50	50% obs	50% obs
A100	100% obs	100% obs
I50	50% obs	Clean
I100	100% obs	Clean
C50	Clean	50% obs
C100	Clean	100% obs

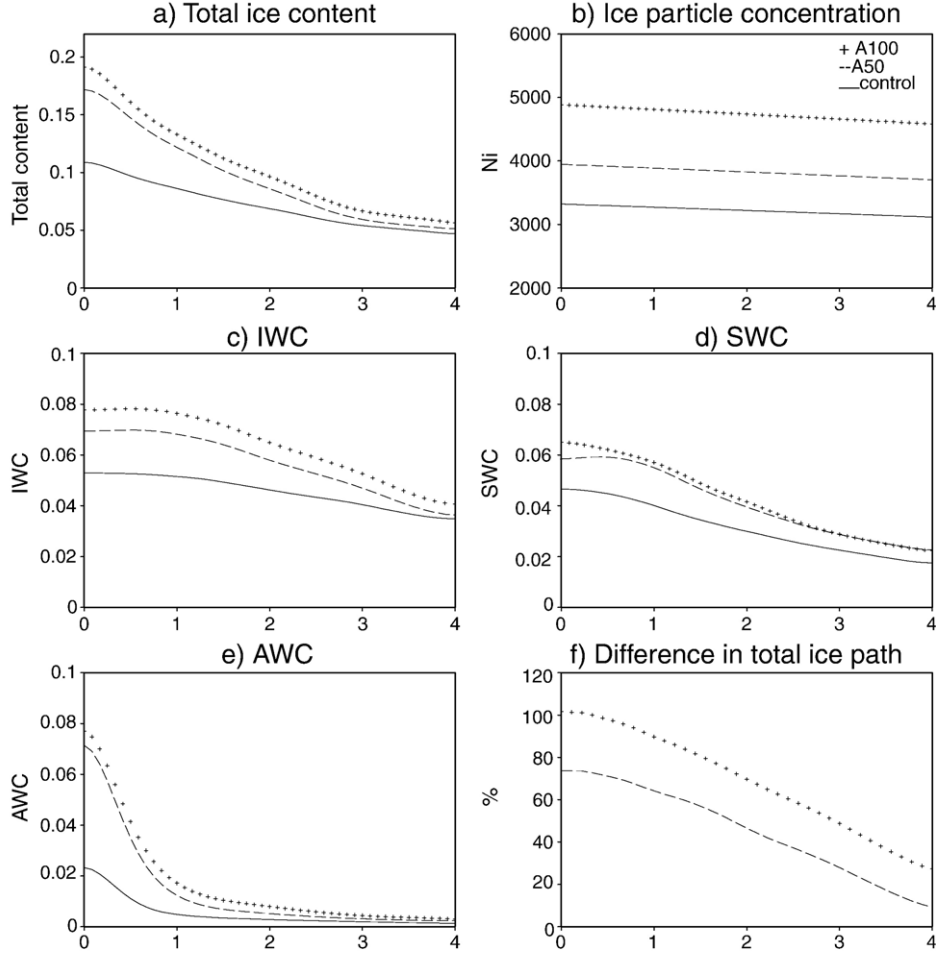


Fig. 8. Temporal evolution of cloud-averaged water contents (gm^{-3}), total ice number concentration (L^{-1}) for A50, A100 and the control run. Percent differences (with respect to the control run) in the total ice water paths simulated for runs A50 and A100 are plotted in panel d. In all panels, abscissas are the simulation time in hours.

Fig. 9c and d for the entire simulation period and for the last hour, respectively. When the entire simulation period was considered, sensitivity experiments showed density function values roughly 30% higher than those corresponding to the control run with a maximum difference for the smallest ice particles (45% for A100). The enhancement in the concentration of small particles was even more important (60% for A100) for the distributions corresponding to the last hour. However, particles with diameters between 40 and 90 μm were less frequent in the sensitivity runs during the fourth hour, after most of the large particles precipitated out of the anvil cloud.

Aircraft measurements were carried out during the dissipation stages of storms for several days during the CRYSTAL-FACE field campaign. Size distribution data

are available for July 18, 2002, the day used by van den Heever et al. (2006) to characterize a clean day concentrations (control run). Unfortunately, there are no aircraft data on ice particle size spectra for July 28, 2002, the day of the simulations (dusty case). However, July 29 could be representative of July 28 as both days were very dusty and had very similar aerosol profiles (DeMott et al., 2003). Moreover, the surface dust concentration in Miami exceeded $30 \mu\text{gm}^{-3}$ and the dust layer reached at times to above 5 km (Sassen et al., 2003) for both days. We generated composite distributions using size distributions obtained by the Citation aircraft above 9 km for July 29 and 18 (courtesy of Andrew Heymsfield). Fig. 10a compares the size distributions of abovementioned composite (July 29) with that modeled for run A100. Both simulated and

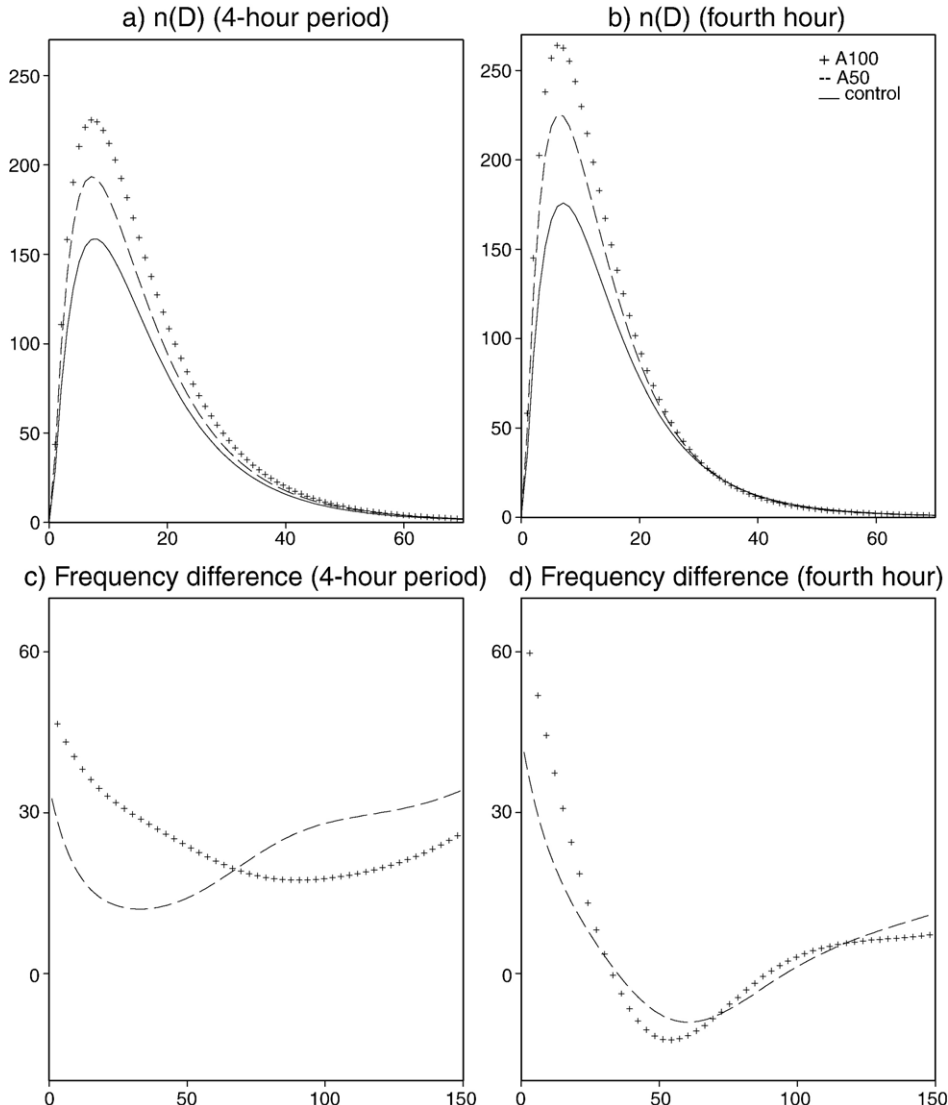


Fig. 9. Comparison size density functions simulated for control for A50, A100 and the control run, corresponding to the 4-hour period and to the fourth hour (a and b, respectively). Percent differences (with respect to the control run) in the density functions simulated for runs A50 and A100 for the same time periods (c and d). In all cases, abscissas are diameters in microns.

observed size distributions show modes at approximately 10 μm . Fig. 10b (analogous to Fig. 9c) gives the percent frequency differences between the composites corresponding to July 29 and July 18 (“dusty” and “clean”, respectively). Positive differences indicate higher ice particle number concentrations for the dusty day.

Fig. 11 compares the temporal evolution of the effective and mean diameters (D_{eff} and D_m) for the same set of runs. Spherical ice particles have been assumed to compute D_{eff} as the size distribution can group particles of different geometry in the same bin. Therefore, D_{eff} was evaluated as the ratio between the third and second

moments of the distribution. As distributions narrowed due to the sedimentation of large ice particles, small ice crystals increasingly dominated the size distributions, and D_{eff} showed a more pronounced decrease with time compared to that of D_m . This behavior was independent of simulation conditions and has been observed for a thunderstorm anvil-cirrus cloud measured on 21 July 2002, also during the CRYSTAL-FACE field campaign (Garrett et al., 2005). When comparing numerical experiments, D_{eff} was 30 and 40% higher than the control run for A50 and A100, respectively. However, as the cloud was advected downwind from the thunderstorm, this difference rapidly became negligible.

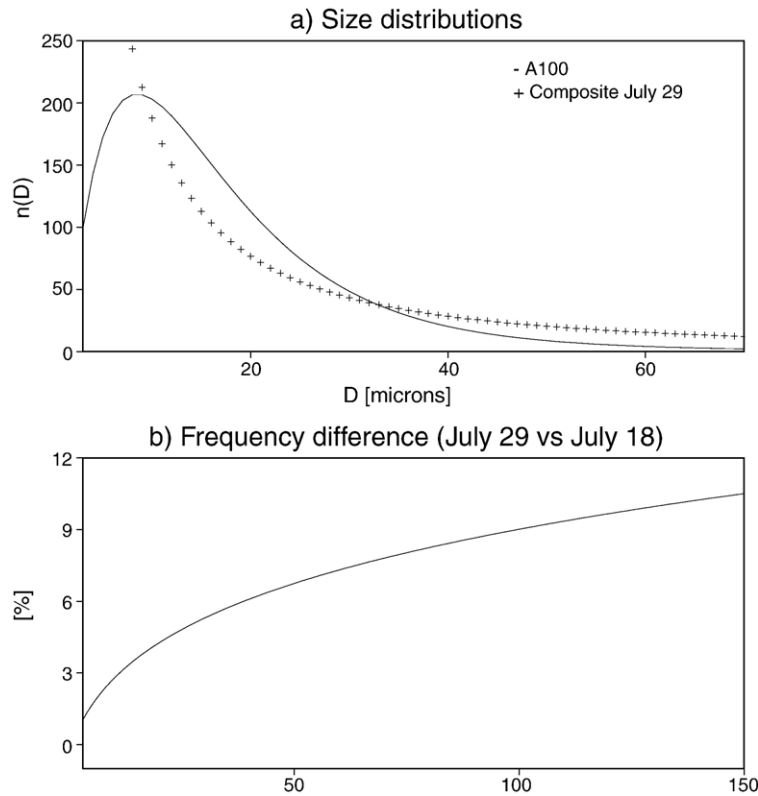


Fig. 10. Comparison between size distributions simulated for run A100 and derived from observations corresponding to July 29, dusty day (a). Percent difference in density functions derived from observations for July 29 and July 18 (dusty day and clean day).

Conversely, the small-diameter range dominated the evolution of D_m with values lower than those of the control run.

As mentioned earlier, enhanced low-level concentration of cloud-nucleating aerosols increased both cloud-averaged ice water contents and ice particle number concentrations in the simulated anvil-cirrus clouds. However, the second moment of the size spectra is a more meaningful quantity to examine the impact on cloud radiative properties. This distribution moment represents the cross-sectional area of ice particles per unit volume of air (optical density) and its vertical integral is proportional to cloud optical depth. The simulated optical density is compared in Fig. 12 for A25, A50, A100, and the control run. In this case, size distributions were computed for approximately 100 cloud levels. Significant change in cloud vertical extension resulted when comparing sensitivity experiments with the control run. Cloud bases were lower due to the increased mass of aggregates precipitating out of the cloud. The slightly higher cloud top at the beginning of the simulations was associated with more intense convection in the sensitivity experiments (see [van den Heever et al. \(2006\)](#) for more details).

After the second hour of simulation, the differences in the cloud vertical extension became negligible. However, the optical density exhibited a monotonic behavior when assuming higher low-level concentration of cloud-nucleating aerosols. The simulated optical density values were significantly higher and the maxima occurred at slightly higher altitudes for A50 and A100.

The downwelling radiative fluxes at the surface, the cloud albedo, as well as the turbulent structure of the simulated clouds were expected to change considering how size spectra varied for the different numerical experiments. Fig. 13 compares the dusty (A100) and the clean (control) runs focusing on the above characteristics. At the beginning of the simulation, the short-wave flux (SWDN) simulated for experiment A100 was significantly lower ($\sim 40 \text{ W m}^{-2}$) than that of the control run (Fig. 13a). Differences naturally decreased in absolute value as the solar day ended approximately 3 h into the simulation. Differences in the long-wave flux (LWDN) were smaller ($\sim 5 \text{ W m}^{-2}$) and opposite in sign (Fig. 13b). The time-averaged vertical profiles of the ratio between shortwave upwelling and downwelling

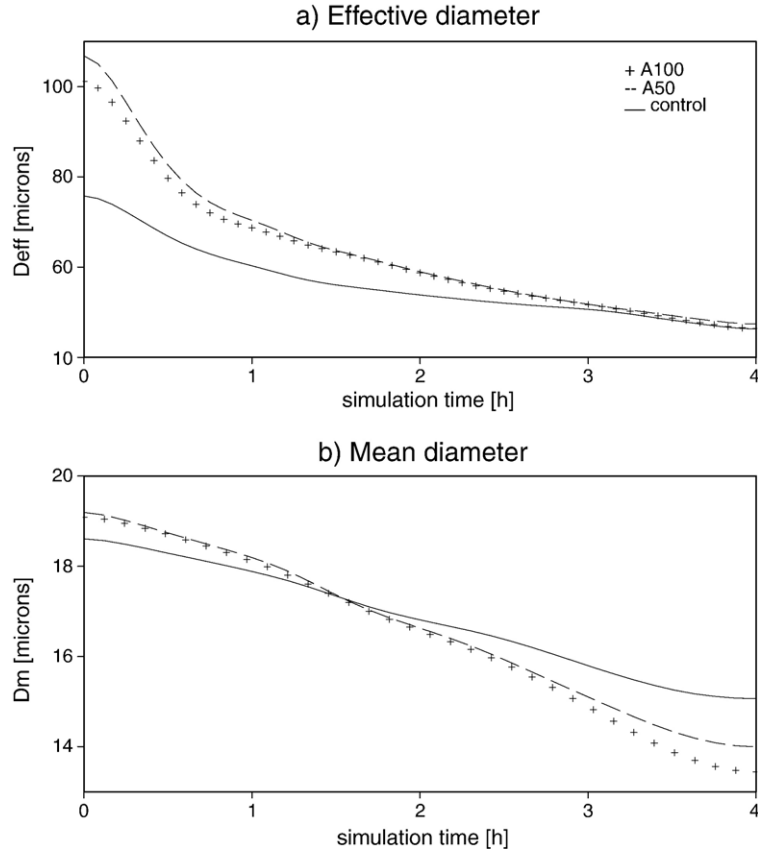


Fig. 11. Temporal evolution of the effective (a) and mean (b) diameter for A50, A100 and the control run.

radiative fluxes are given in Fig. 13c. The value of this ratio at the top of the cloud represents cloud albedo and for the dusty run, it was approximately 10% larger than that of the clean one. Simulated cloud albedo showed a monotonic behavior when comparing the control run and experiments A25, A50, and A100 (not shown). Fig. 13d compares the probability density functions (PDFs) of the turbulent kinetic energy (TKE) for the 4-hour simulation period. The PDFs considered both the resolved and parameterized (subgrid) values, although subgrid-scale TKE was comparatively negligible. Velocity perturbations were computed using 5-min outputs of the resolved 3-D velocity field, and they were defined with respect to the horizontally averaged values for the corresponding time and model level. It can be seen that large values of TKE were less frequent for the sensitivity experiments indicating a less turbulent cloud. This latter difference in conjunction with the impact on ice water contents and the size spectra suggests a significant increase in the lifetime of anvil-cirrus clouds.

As mentioned in Section 3, we performed various runs that enhanced only the concentrations of CCN or

IFN. Figs. 14 and 15 are completely analogous to Fig. 8 but for experiments that consider environments polluted only in terms of CCN and IFN, respectively. When enhancing only CCN concentrations, the general response of the model was similar to that of enhancing both IFN and CCN (compare Figs. 8 and 14). As in runs A50 and A100, greater amounts of supercooled liquid water reached high levels of the convective cloud, facilitating the homogeneous freezing of pristine ice, the riming of snow, and the formation of aggregates. However, the impacts on IWC, SWC and AWC and N_i were slightly less important (compared with A50 and A100). A lower number of pristine ice crystals formed by deposition-condensation freezing as clean IFN concentrations were assumed for runs C150 and C100. For the runs I50 and I100 (Fig. 14) that only varied IFN concentrations, simulated water contents and N_i were higher than those of the control run, although differences were significantly smaller. N_i did not exhibit a monotonic behavior. No significant changes in AWC resulted for runs I50 and I100. Supercooled droplets reaching high altitudes in the convective cloud are

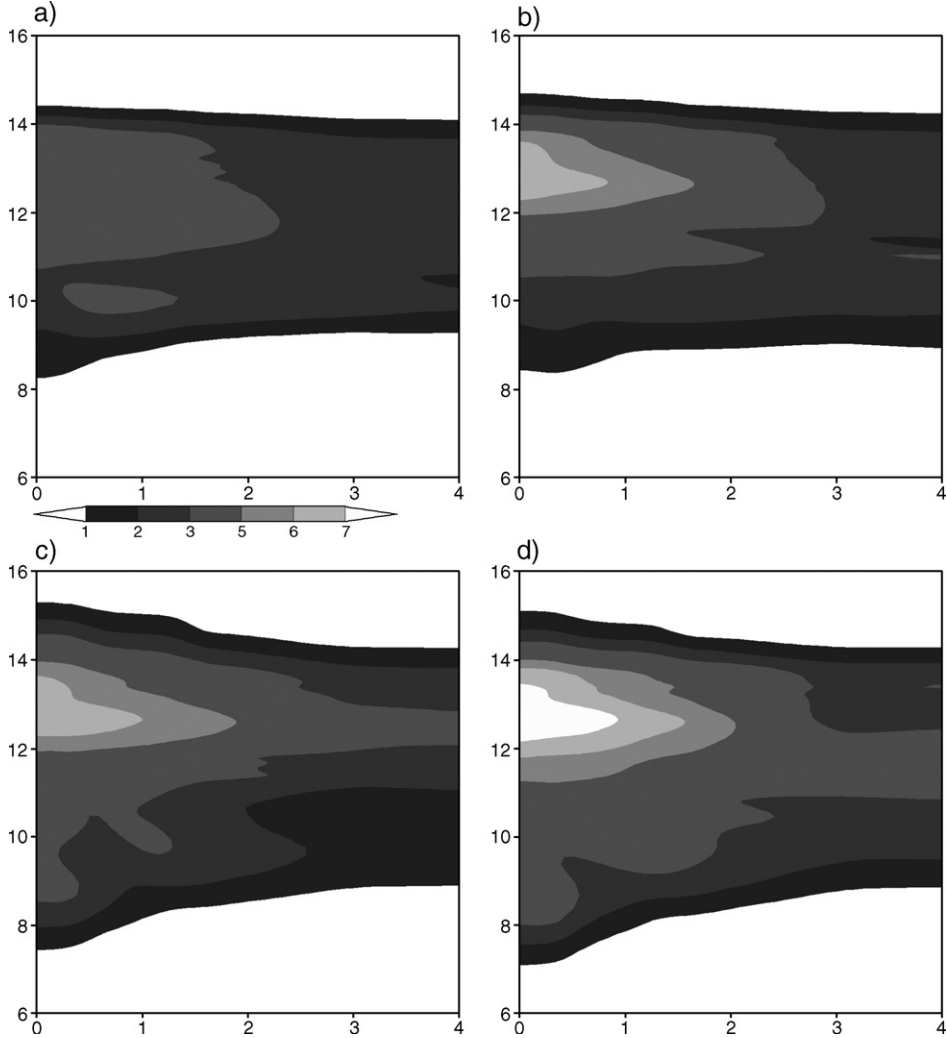


Fig. 12. Horizontally averaged optical density ($10^{-3} \times m^{-1}$) for the control run (a), A25 (b), A50 (c), and A100 (d). Ordinates represent altitude in kilometers and abscissas, the simulation time in hours.

necessary for the formation of aggregates transported to the outflow (see van den Heever et al., 2006). With clean CCN concentrations, the liquid mass was distributed in a lower number of larger cloud droplets that freeze at warmer temperatures, and the larger cloud droplets were more efficiently removed by collisional mechanisms therefore less likely to reach higher levels of the convective cloud.

The effects of enhancing IFN, CCN or both types of aerosols on the time-averaged total condensate path (TCP, that considers all ice-phase species) are compared in Table 2. This table shows the percent changes in TCP with respect to the control run (Δ_m), as well as the time-averaged mass fractions corresponding to pristine ice, snow crystals, and aggregates. All values shown in this table represent temporal averages over the entire

simulation period. All sensitivity runs showed a significant increase in TCP, although the change was more significant for A100 and C100. The run based on the observed IFN and CCN profiles (A100) had the largest fraction of particles that has been involved in collisions (aggregates). The lowest percentage of crystals that only grew by vapor diffusion (pristine ice) also corresponded to run A100. Conversely, I100 had the largest mass fraction of pristine ice, probably due to enhanced deposition-condensation freezing in the convective cloud and a reduced rate of aggregation within the outflow.

The temporal evolution of the ice particle size distributions is compared for the control, I100, C100, and A100 runs, in Fig. 16a, b, c, and d, respectively. These density functions were evaluated every 5 min

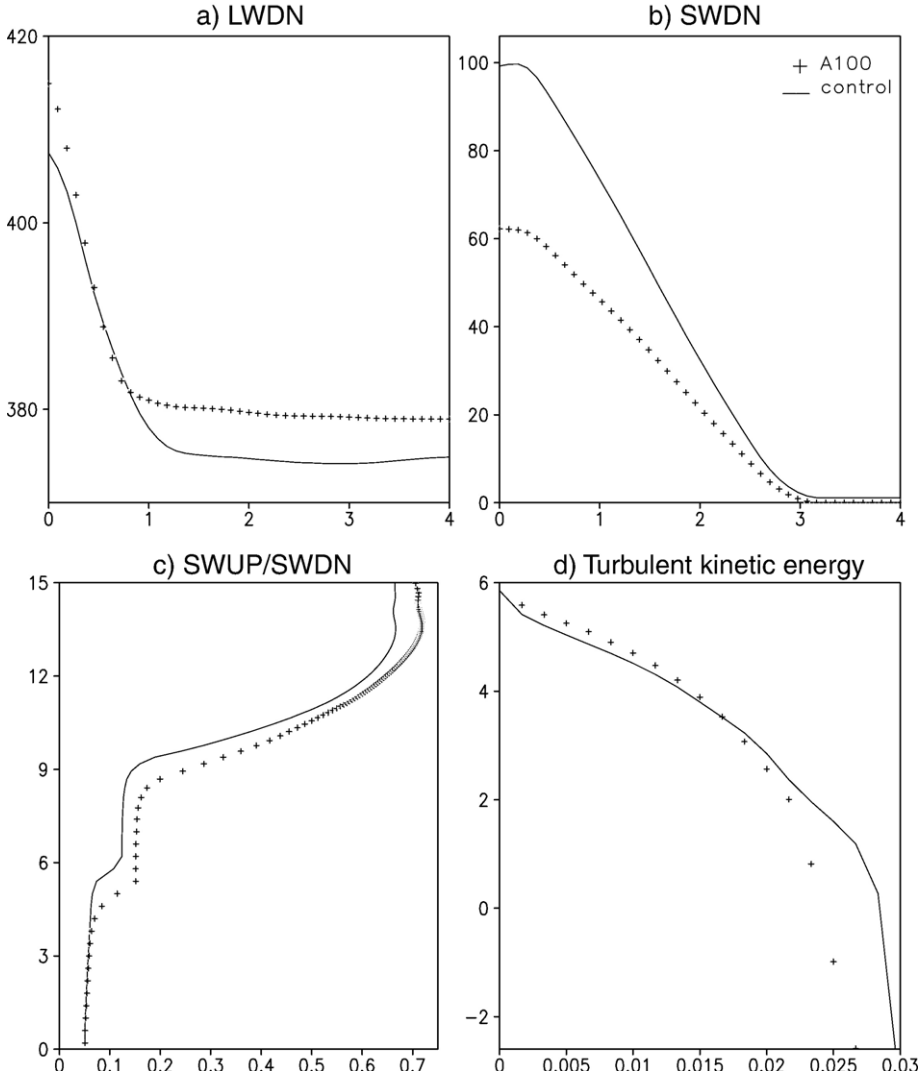


Fig. 13. Horizontally averaged longwave and shortwave fluxes at the surface (a, b). In panels a and b, ordinates represent the downwelling fluxes (W m^{-2}) and abscissas, the simulation time in hours. Panel c gives the ratio between SWUP and SWDN (the ordinate is altitude in km). Probability density function for TKE is plotted in panel d (the ordinate is $\log(\text{PDF})$ while the abscissa is TKE in m^2/s^2).

using output data corresponding to every cloudy grid cell and all ice-phase species. All sensitivity experiments showed a significant enhancement in the concentration of particles with sizes below 20 μm in diameter. This difference was most important for run A100 (followed by C100), although it exhibited a negligible change at the tail of the distribution after the third hour. Conversely, enhancing only IFN concentrations had the least important impact on the concentration of small ice particles, although it produced the widest size distribution at the end of the simulation period. The profiles of the optical density corresponding to the 4-h simulation period are plotted in Fig. 17 for A100, C100, I100 and the control run. This density was evaluated for

each altitude as the second order moment of the size distribution at the corresponding model level. The layer with high optical densities for C100 and I100 was thinner compared to A100. For this reason, the latter generated the optically thickest anvil-cirrus cloud, even when the maximum simulated density corresponded to C100.

We compared the ice particle concentration (zeroth moment, M^0), the mean diameter (M^1/M^0), the effective diameter ($\sim M^3/M^2$), and the second moment (proportional to the optical depth) for various runs. Percent differences with respect to the control run are given in Table 3. The first five columns of this table represent quantities temporally averaged over the 4 hour-period,

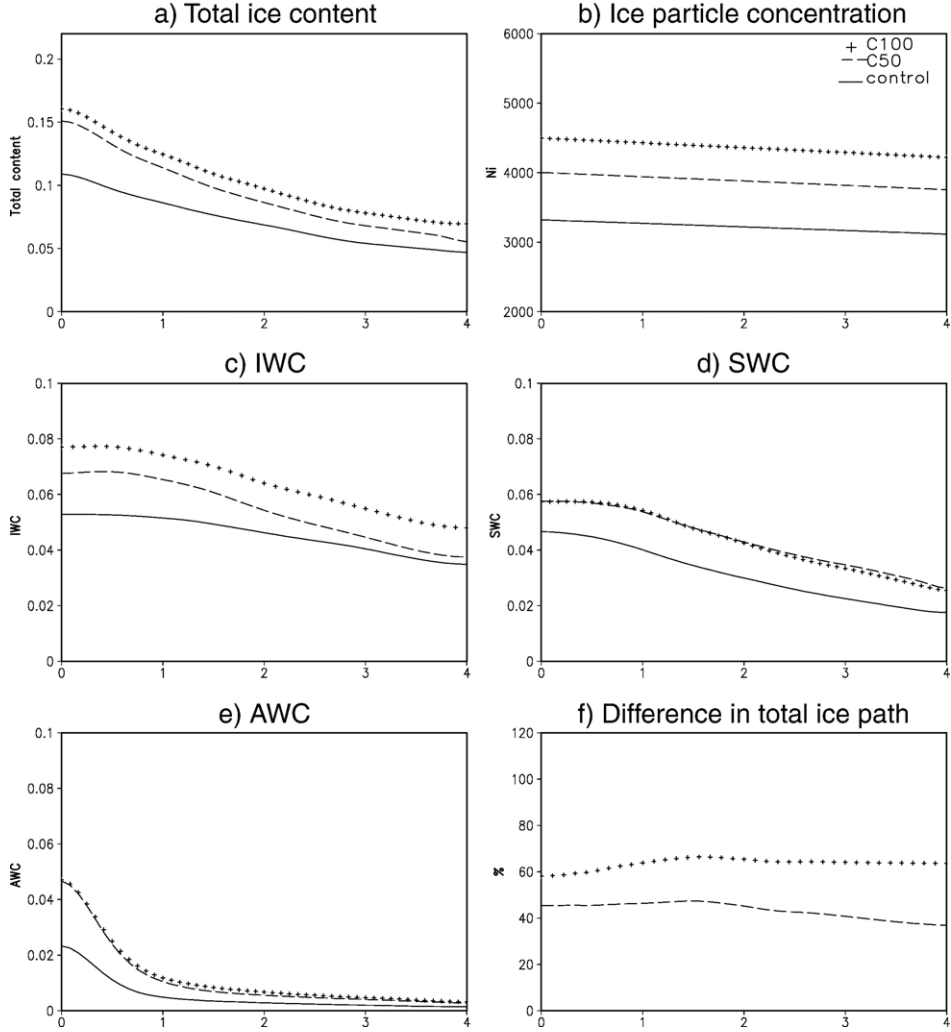


Fig. 14. Temporal evolution of cloud-averaged water contents (gm^{-3}), total ice number concentration (L^{-1}) for C50, C100 and the control run. Percent differences (with respect to the control run) in the total ice water paths simulated for runs C50 and C100 are plotted in panel (d). In all cases, abscissa is simulation time in hours.

while the sixth column corresponds to averages over the fourth hour only. As mentioned in Section 3.2, we performed two 8-hour simulations, completely analogous to the control and A100 runs but using grid 2 to extend trajectories and large-scale tendencies. The last column of Table 3 represents quantities temporally averaged over this extended 8-hour period. Enhancing aerosol concentrations monotonically increased the number concentration, the effective diameter, and the cloud optical depth. A slight reduction in the mean diameter can also be seen when comparing runs A25, A50, and A100 (see also A100 for the fourth hour). Experiment C100 exhibited a similar behavior with a large increase in M^0 and the effective diameter and small (but positive) change in mean diameter. Con-

versely, enhancing only IFN concentrations produced larger particles and the increase in ice particle number concentration was less important. Finally, for the extended simulation period, enhancing low-level cloud-nucleating aerosol concentrations produced cirrus-anvil clouds with optical depths approximately 24% higher than those corresponding to a clean day (control run).

5. Summary and conclusions

The results of a series of Large Eddy Simulations (LES) which were performed to examine the sensitivity of anvil-cirrus clouds to variations in the concentration of nucleating aerosols entrained in cumulonimbi have

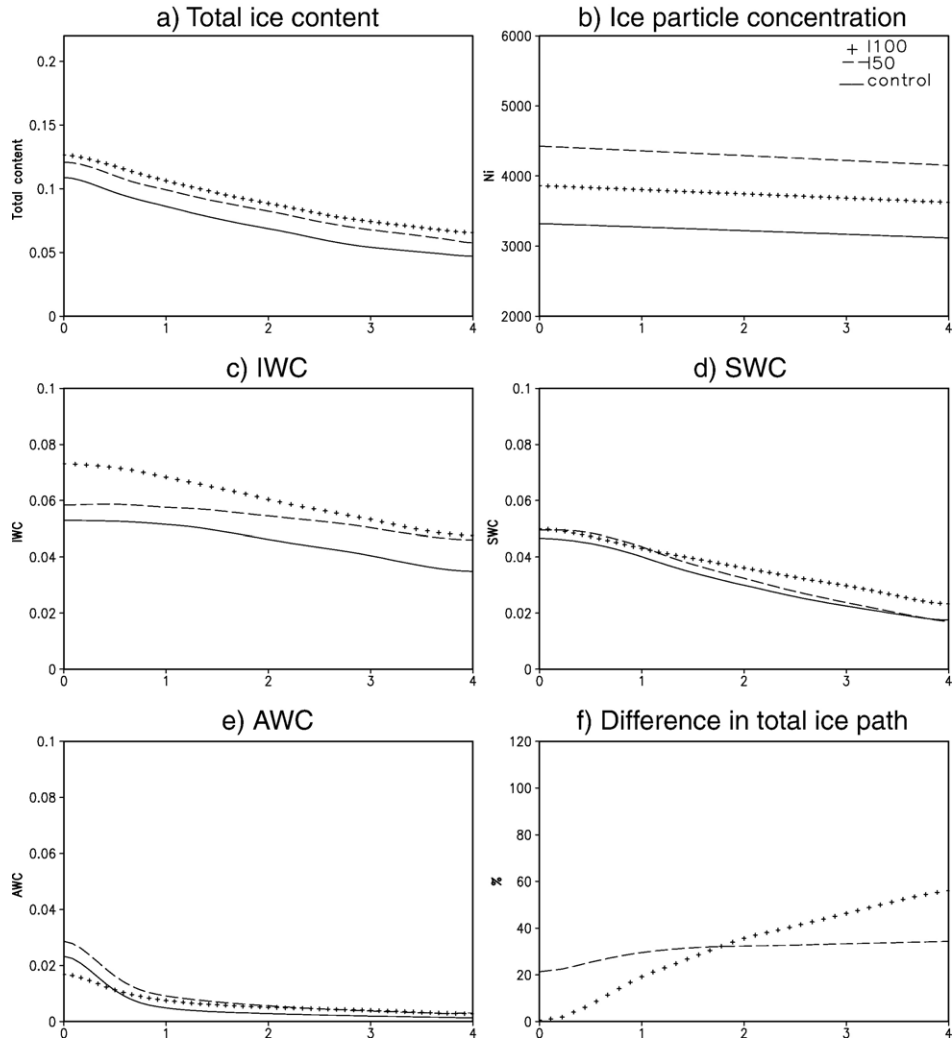


Fig. 15. Idem Fig. 14 but for or I50, I100 and the control run.

been presented. These high-resolution simulations represent an adequate framework to simulate the microphysical, radiative and dynamical processes governing the evolution of these type of clouds after they detach from the storm outflow. A series of mesoscale simulations (van den Heever et al., 2006) provided

Table 2
Mass fractions of each ice-phase species for the 4-hour period

	Pristine [%]	Snow [%]	Aggregates [%]	Δ_m [%]
Control	58.84	35.46	5.7	
I100	61.77	32.37	5.86	31.98
C100	57.33	33.85	8.82	63.51
A100	55.16	33.29	11.55	68.41

The last column gives percent difference in the total condensate path with respect to the control run.

initialization and large-scale tendencies for the LES moving domain.

Based on the results of their modeling study of storms that developed during CRYSTAL-FACE, Friedlind et al. (2004) advanced the hypothesis that aerosols between 6 and 10 km had the greatest impact on the cirrus anvil microphysics. However, our simulations demonstrate that many characteristics of both the convective and anvil stages of storm development are sensitive to changes in the aerosol concentrations below 4 km. It must be noted that we focused on changes in the water mass (and ice particle size distributions) transported to cirrus-anvil levels due to varying lower-tropospheric aerosol.

The effect of enhancing aerosol concentrations resulted in cirrus-anvil clouds that are physically and

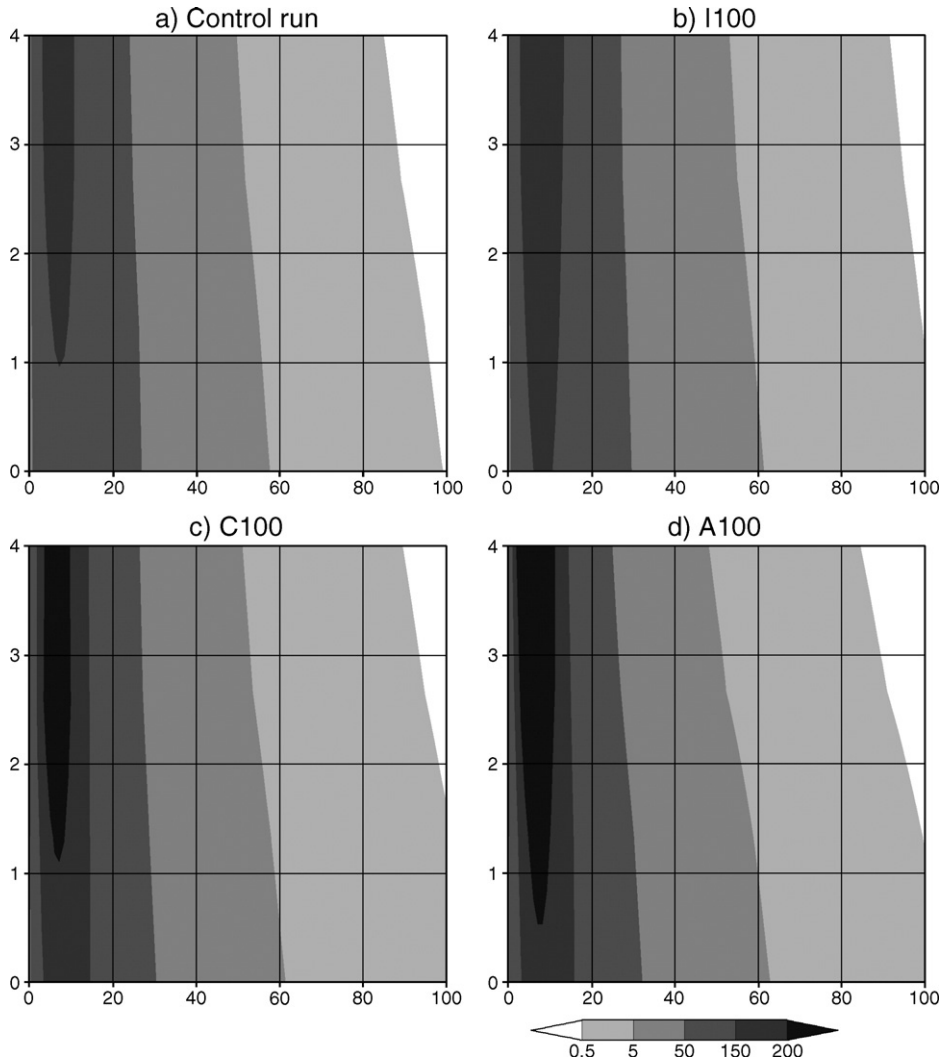


Fig. 16. The temporal evolution of the ice particle size distributions for the control, A25, A50, and A100 runs (a, b, c, and d, respectively). The abscissas are diameters in microns, and the ordinates, the simulation time in hours.

optically thicker. The largest differences in optical depth ($\sim 40\%$), cloud-averaged effective diameter ($>25\%$), and ice water content ($\sim 75\%$) occurred during the first hours of simulation due to a higher frequency of large particles (aggregates). These differences rapidly decreased in magnitude as size distributions narrowed with time due to the sedimentation of aggregates. During the last hour of the simulations, the cloud-averaged effective diameter showed no significant change with respect to the control run, and the mean diameter decreases. However, due to the fact that differences in ice particle number concentrations were large ($>30\%$) during the entire 4-hour simulation period, the impact on optical depth remained important. It is interesting to note that, most of the abovementioned

microphysical quantities, as well as optical properties (including cloud reflectivity), showed a clearly monotonic behavior when assuming environments more polluted in terms of aerosols.

For those sensitivity experiments designed to isolate the impact of enhancing only low-level CCN concentrations, the general response of the model was very similar to that described in the previous paragraph, although differences with respect to the control run were slightly smaller. For both sets of runs, the mass fraction of ice particles that were involved in collisions (aggregates) and total ice number concentrations exhibited a monotonic behavior, while ice crystals that only grew by vapor diffusion (pristine ice) showed no significant changes. Conversely, enhancing IFN concentrations had an

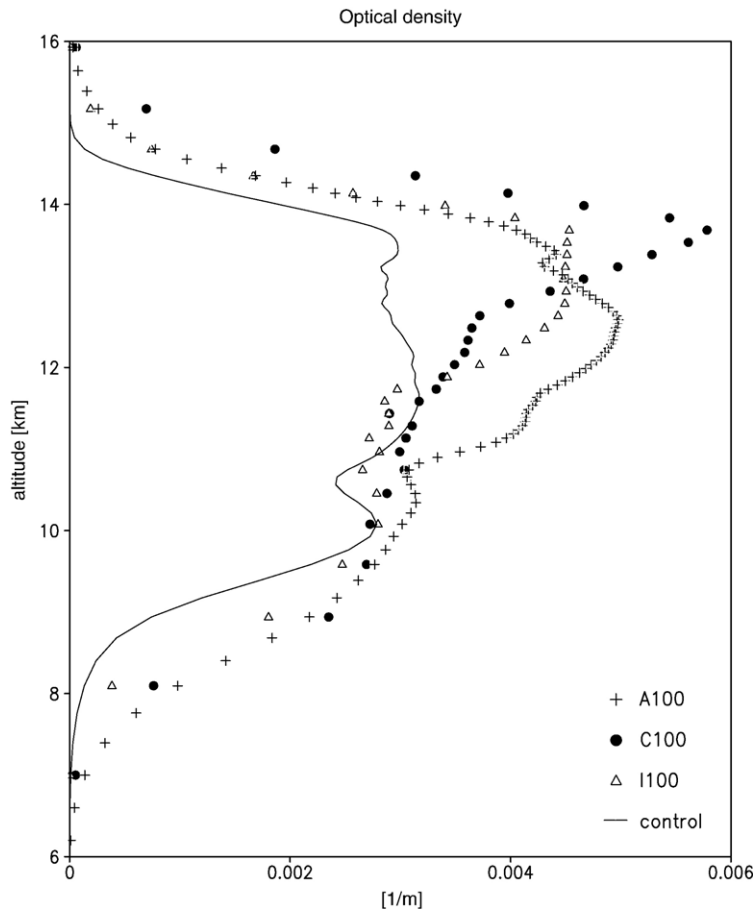


Fig. 17. Horizontally and time-averaged optical density (m^{-1}) profiles for A100, C100, I100, and the control run.

important impact on the mass fraction of pristine ice but a negligible effect on aggregates. Enhanced IFN concentrations resulted in narrower size distributions and larger mean diameters. The increase in total ice number concentration was less important ($\sim 15\%$) and this quantity showed no monotonic response when assuming higher IFN concentrations.

The differences in the simulated size distributions can be explained if we consider that enhancing CCN concentrations has two different effects. A larger number of (smaller) supercooled cloud droplets reaches the top of the convective cloud, significantly increasing the number concentration of ice particles with diameters less than $20 \mu\text{m}$ (Rosenfeld and Woodley, 2000; Khain et al., 2001). A significantly larger number of cloud droplets at high levels of the convective cloud would also increase the probability of binary interactions and therefore the production of aggregates, explaining the difference in the tail of the distributions. As we mentioned in Section 4, the largest differences in the size distributions corresponded to the numerical experi-

ment that enhanced both IFN and CCN concentrations. Another contribution to the concentration of small ice particles can be associated with a greater production of pristine ice crystals when we enhanced IFN concentrations as well as CCN concentrations. The larger concentration of pristine ice crystals would also increase the production of aggregates.

In summary, the enhancements of both IFN and CCN showed important effects on ice particle size spectra of simulated anvil-cirrus clouds. Our results suggest that the influence of CCN is dominant. A cooling effect can

Table 3
Comparison of distribution moments computed for different runs and time-averaging periods

	I100	C100	A25	A50	A100	A100 4th h	A100 8 h sim
M^0	15.8	28.8	5.7	18.1	36.8	33.7	35.2
M^1/M^0	4.7	1.1	4.0	-1.6	-2.7	-8.6	-5.6
M^3/M^2	0.3	11.0	10.2	18.4	15.6	1.9	8.7
M^2	24.6	29.3	16.8	20.7	33.5	13.9	23.9

be associated with Saharan dust intrusions as the optical thickness and cloud albedo increase when assuming enhanced concentrations of low-level cloud-nucleating aerosols. Moreover, narrower ice particle size distributions and lower turbulent kinetic energy suggest the lifetime of anvil-cirrus clouds is increased.

Acknowledgements

Gustavo Carrió, Susan van den Heever, and William Cotton were funded by the National Aeronautical Space Administration under Contracts NAG5-11507 and NNG04GG44G. The authors also wish to thank Andrew Heymsfield for providing ice crystal size-distribution observational data, Paul DeMott and William Cheng for useful discussions, Louis Nguyen for the visible satellite images, and Brenda Thompson for technical support.

References

- Brown, P.R.A., Heymsfield, A.J., 2001. The microphysical properties of tropical convective anvil cirrus: a comparison of models and observations. *Quart. J. R. Met. Soc.* 127, 1535–1550.
- Carrió, G.G., Jiang, H., Cotton, W.M., 2005a. Impact of aerosol intrusions on Arctic boundary layer clouds: Part I. May 4 1998 case. *J. Atmos. Sci.* 62, 3082–3093.
- Carrió, G.G., Jiang, H., Cotton, W.M., 2005b. Impact of aerosol intrusions on Arctic boundary layer clouds: Part II. Sea-ice melting rates. *J. Atmos. Sci.* 62, 3094–3105.
- Cheng, W.Y.Y., Wu, T., Cotton, W.R., 2001. Large-eddy simulations of the 26 November 1991 FIRE II cirrus case. *J. Atmos. Sci.* 58, 1017–1034.
- Chiapello, I., Moulin, C., Prospero, J.M., 2005. Understanding the long-term variability of African dust transport across the Atlantic as recorded in both Barbados surface concentrations and large-scale Total Ozone Mapping Spectrometer (TOMS) optical thickness. *J. Geophys. Res.* 110, D18S10. doi:10.1029/2004JD005132.
- Chou, M.-D., Lindzen, R.S., Hou, A.Y., 2002. Comments on the iris hypothesis: a negative or positive cloud feedback? *J. Climate* 15, 2713–2715.
- Cotton, W.R., Pielke Sr., R.A., Walko, R.L., Liston, G.E., Tremback, C.J., Jiang, H., McAnelly, R.L., Harrington, J.Y., Nicholls, M.E., Carrió, G.G., Mc Fadden, J.P., 2003. RAMS 2001: current status and future directions. *Meteorol. Atmos. Phys.* 82, 5–29.
- DeMott, P.J., Meyers, M.P., Cotton, W.R., 1994. Parameterization and impact of ice initiation processes relevant to numerical model simulations of cirrus clouds. *J. Atmos. Sci.* 51, 77–90.
- DeMott, P.J., Sassen, K., Poellet, M.R., Baumgardner, D., Rogers, D. C., Brooks, S.D., Prenni, A.J., Kreidenweis, S.M., 2003. African dust aerosols as atmospheric ice nuclei. *Geophys. Res. Lett.* 30, 1732. doi:10.1029/2003GL017410.
- Feingold, G., Stevens, B., Cotton, W.R., Walko, R.L., 1994. An explicit cloud microphysical/LES model designed to simulate the Twomey effect. *Atmos. Res.* 33, 207–233.
- Fowler, L.D., Randall, D.A., 1994. A global radiative-convective feedback. *Geophys. Res. Lett.* 21, 2035–2038.
- Fridlind, A.M., A. S. Ackerman, E. J. Jensen, A. J. Heymsfield, M. R. Poellot, D. E. Stevens, D. Wang, L. M. Miloshevich, D. Baumgardner, R. P. Lawson, J. C. Wilson, R. C. Flagan, J. H. Seinfeld, H. H. Jonsson, T. M. VanReken, V. Varutbangkul, and T. Fu, A., Krueger, S.K., Liou, K.N., 1995. Interactions of radiation and convection in simulated tropical cloud clusters. *J. Atmos. Sci.* 52, 1310–1328.
- Garrett, T.J., Navarro, B.C., Twohy, C.H., Jensen, E.J., Baumgardner, D.G., Bui, T.P., Gerber, H., Herman, R.L., Heymsfield, A.J., Lawson, P., Minnis, P., Nguyen, L., Poellot, M., Pope, S.K., Valero, F.P.J., Weinstock, E., 2005. Evolution of a Florida cirrus anvil. *J. Atmos. Sci.* 62, 2352–2372.
- Jensen, E.J., Kinne, S., Toon, O.B., 1994. Tropical cirrus cloud radiative forcing: sensitivity studies. *Geophys. Res. Lett.* 21, 2023–2026.
- Harrington, Y.Y., Reisin, T., Cotton, W.R., Kreidenweis, S.M., 1999. Cloud resolving simulations of Arctic stratus: Part II. Transition-season clouds. *Atmos. Res.* 51, 45–75.
- Hobbs, P.V., Politovich, M.K., Radke, L.F., 1980. The structures of summer convective clouds in eastern Montana: I. Natural clouds. *J. Appl. Meteorol.* 19, 645–663.
- Jiang, H., Cotton, W.R., Pinto, J.O., Curry, J.A., Weissbluth, M.J., 2000. Cloud resolving simulations of mixed-phase Arctic stratus observed during BASE: sensitivity to concentration of ice crystals and large-scale heat and moisture advection. *J. Atmos. Sci.* 57, 2105–2117.
- Jiang, H., Feingold, G., Cotton, W.R., Duynkerke, P.G., 2001. Large-eddy simulations of entrainment of cloud condensation nuclei into the Arctic boundary layer: May 18, 1998, FIRE/SHEBA case study. *J. Geophys. Res.* 106 (15), 113–115 (122).
- Khain, A.P., Rosenfeld, D., Pokrovsky, A., 2001. Simulating convective clouds with sustained supercooled liquid water down to -37.5°C using a spectral microphysics model. *Geophys. Res. Lett.* 28, 3887–3890.
- Krueger, S.K., Fu, Q., Liou, K.N., Chin, H.-N.S., 1995. Improvements of an ice-phase microphysics parameterization for use in numerical simulations of tropical convection. *J. Appl. Meteorol.* 34, 281–287.
- Lin, B., Wielicki, B., Chambers, L., Hu, Y., Xu, K.-M., 2002. The iris hypothesis: a negative or positive cloud feedback? *J. Climate* 15, 3–7.
- Meyers, M.P., Walko, R.L., Harrington, J.Y., Cotton, W.R., 1997. New RAMS cloud microphysics parameterization: Part II. The two-moment scheme. *Atmos. Res.* 45, 3–39.
- Mitchell, D.L., Macke, A., Liu, Y., 1996. Modeling cirrus clouds: Part II. Treatment of radiative properties. *J. Atmos. Sci.* 53, 2967–2988.
- Mossop, S.C., 1978. The influence of drop size distribution on the production of secondary ice particles during graupel growth. *Quart. J. R. Met. Soc.* 104, 323–330.
- Pielke, R.A., Cotton, W.R., Walko, R.L., Tremback, C.J., Lyons, W.A., Grasso, L.D., Ritter, B., Geleyn, J.F., 1992. A comprehensive radiation scheme for numerical weather prediction models with potential applications in climate simulations. *Mon. Weather Rev.* 120, 303–325.
- Platt, C.M.R., 1989. The role of cloud microphysics in high-cloud feedback effects on climate change. *Nature* 341, 428–429.
- Platt, C.M.R., Harshvardhan, 1988. Temperature dependence of cirrus extinction: implications for climate feedback. *J. Geophys. Res.* 93, 11051–11058.
- Ramanathan, V., Collins, W., 1991. Thermodynamic regulation of ocean warming by cirrus clouds deduced from observations of the 1987 El Niño. *Nature* 351, 27–32.

- Ritter, B., Geleyn, J.F., 1992. A comprehensive radiation scheme for numerical weather prediction models with potential applications in climate simulations. *Mon. Wea. Rev.* 120, 303–325.
- Rosenfeld, D., Woodley, W.L., 2000. Deep convective clouds with sustained supercooled liquid water down to -37.5°C . *Nature* 405, 440–442.
- Saleeby, S.M., Cotton, W.R., 2003. A large-droplet model and prognostic number concentration of cloud droplets in the RAMS@CSU model: Part I. Module descriptions and Supercell test simulations. *J. Appl. Meteorol.* 43, 182–195.
- Sassen, K., DeMott, P.J., Prospero, J.M., Poellet, M.R., 2003. Saharan dust storms and indirect aerosol effects on clouds: CRYSTALFACE results. *Geophys. Res. Lett.* 30, 1633. doi:[10.1029/2003GL017371](https://doi.org/10.1029/2003GL017371).
- Slingo, A., Schrecker, H.M., 1982. On the shortwave radiative properties of stratiform water clouds. *Quart. J. R. Met. Soc.* 108, 407–426.
- Starr, D.O.C., Cox, S.K., 1985. Cirrus clouds, Part II: Numerical experiments on the formation and maintenance of cirrus. *J. Atmos. Sci.* 42, 2682–2694.
- Stephens, G.L., 1998. Cirrus clouds and global change. *Proc. Cirrus Tropical Meeting*. OSA/AGU, Baltimore, MD, pp. 154–156.
- van den Heever, S.C., Carrió, G.G., Cotton, W.R., DeMott, P.J., Prenni, A.J., 2006. Impacts of nucleating aerosol on Florida convection: Part I. Mesoscale simulations. *J. Atmos. Sci.* 63, 1752–1775.